Asymmetric nanotopography biases cytoskeletal dynamics and promotes unidirectional cell guidance

Xiaoyu Sun[a], Meghan K. Driscoll[b,c], Can Guven[b,c], Satarupa Das[c], Carole A. Parent[d], John T. Fourkas[a,e,1], and Wolfgang Losert[b,c,e,1]

[a]Department of Chemistry and Biochemistry, University of Maryland, College Park, MD 20742; [b]Department of Physics, University of Maryland, College Park, MD 20742; [c]The Institute for Research in Electronics and Applied Physics, University of Maryland, College Park, MD 20742; [d]Laboratory of Cellular and Molecular Biology, Center for Cancer Research, National Cancer Institute, National Institutes of Health, Bethesda, MD 20892; and [e]Institute for Physical Science and Technology, University of Maryland, College Park, MD 20742

Edited by Thomas D. Pollard, Yale University, New Haven, CT, and approved September 1, 2015 (received for review February 12, 2015)

Many biological and physiological processes depend upon directed migration of cells, which is typically mediated by chemical or physical gradients or by signal relay. Here we show that cells can be guided in a single preferred direction based solely on local asymmetries in nano/microtopography on subcellular scales. These asymmetries can be repeated, and thereby provide directional guidance, over arbitrarily large areas. The direction and strength of the guidance is sensitive to the details of the nano/microtopography, suggesting that this phenomenon plays a context-dependent role in vivo. We demonstrate that appropriate asymmetric nano/microtopography can unidirectionally bias internal actin polymerization waves and that cells move with the same preferred direction as these waves. This phenomenon is observed both for the pseudopod-dominated migration of the amoeboid *Dictyostelium discoideum* and for the lamellipod-driven migration of human neutrophils. The conservation of this mechanism across cell types and the asymmetric shape of many natural scaffolds suggest that actin-wave-based guidance is important in biology and physiology.

cell migration | actin waves | contact guidance | *Dictyostelium discoideum* | neutrophils

Directed cell migration is essential for many critical biological and physiological processes (1), such as embryonic development (2), wound healing (3), immune response (4), and angiogenesis (5). Guidance of cells can be achieved through external gradients in properties such as chemical concentration (6, 7), substrate rigidity (8), and adhesion (9). The total distance over which gradients can guide cells is limited by the finite dynamic range of cellular sensing [i.e., guidance by a gradient between the front and back of each cell requires that the overall signal change significantly with the cell's position (Fig. 1*A*)]. Cells can overcome this limitation by relaying chemotactic signals, but chemical relay of directional information requires intricate orchestration and timing of signals (7, 10, 11). Shear flow is another approach to guiding cells unidirectionally over large distances, but shear flow is an active process that requires constant fluid flow at a controlled rate and viscosity (12, 13). Surface nanotopography, such as ridges and grooves (14–17) or aligned collagen fibers (18), can act as a primitive and ubiquitous guidance cue, but the symmetric structures used in prior studies only provided bidirectional guidance.

Although previous work has implicated cytoskeletal structures [in particular, the alignment of stress fibers (16)] in similar contact guidance processes, we have recently shown that nanotopography also steers the dynamics of the cell's scaffolding by biasing actin polymerization waves (17). Intracellular dynamics involving the self-assembly of actin and actin's associated proteins into 3D, traveling waves that propel a cell forward through a sustained cycle of polymerization and depolymerization have recently been found to be ubiquitous in cell migration (19–22). Given that nano/microtopographies in natural and physiological environments, often include asymmetric structures (as is the case, for example, in collagen fibers), we hypothesized that nano/microtopographic asymmetries on an appropriate length scale can bias actin waves and cell migration unidirectionally. To distinguish guidance induced by underlying nano/microtopographies on a subcellular scale from other gradient-sensing mechanisms, we term this topographic guidance phenomenon "microthigmotaxis" (with "thigmo" being Greek for "touch").

Results and Discussion

We used surfaces composed of parallel ridges of sawteeth (Fig. 1*B* and Movie S1) to induce unidirectional guidance of cells. Although the length and height of the sawteeth reach more than 1 μm, the nanoscale features of the topography, in particular the width and radius of curvature of the sawtooth ridges, are critical for nucleating and guiding actin polymerization, the key internal guidance mechanism. We investigated in two prototypical cell types that move via amoeboid migration: *Dictyostelium discoideum*, which migrates using pseudopods that protrude away from surface contacts, and neutrophils, which migrate using lamellipodia that spread along surface contacts. The sawtooth dimensions (length, height, and width) and the spacing between adjacent sawtooth ridges are all comparable in size to natural collagen fibers (18) and are considerably smaller than the dimensions of an individual cell (the average width of a polarized cell is 5 μm for *D. discoideum* and 10 μm for neutrophils). Thus, individual cells span several ridges and many sawteeth (Fig. 1*C*).

To explore how *D. discoideum* conforms to sawteeth, we visualized YFP-labeled cAR1 (cyclic AMP receptor 1) cells, which express

Significance

Directed motion of cells is essential to many natural and physiological processes, including development and wound healing. Although gradients in chemical or physical properties are well known to guide cells, gradients that are strong enough to guide cells can only cover limited distances. Here we demonstrate that materials with local asymmetries in nano/microtopography on subcellular scales are able to guide cells with a single preferred direction. Unlike conventional gradients, local asymmetries on subcellular scales can be repeated over arbitrarily large regions, providing directional guidance over an unlimited range. This unidirectional guidance is mediated by biasing of the direction of waves of polymerization of the cell's actin scaffolding, a mechanism that is conserved from primitive cells to human cells.

Author contributions: X.S., M.K.D., J.T.F., and W.L. designed research; X.S. and S.D. performed research; M.K.D. and C.G. contributed new reagents/analytic tools; X.S., M.K.D., C.G., and C.A.P. analyzed data; and X.S., M.K.D., C.G., S.D., C.A.P., J.T.F., and W.L. wrote the paper.

The authors declare no conflict of interest.

This article is a PNAS Direct Submission.

Freely available online through the PNAS open access option.

[1]To whom correspondence may be addressed. Email: fourkas@umd.edu or wlosert@umd.edu.

This article contains supporting information online at www.pnas.org/lookup/suppl/doi:10.1073/pnas.1502970112/-/DCSupplemental.

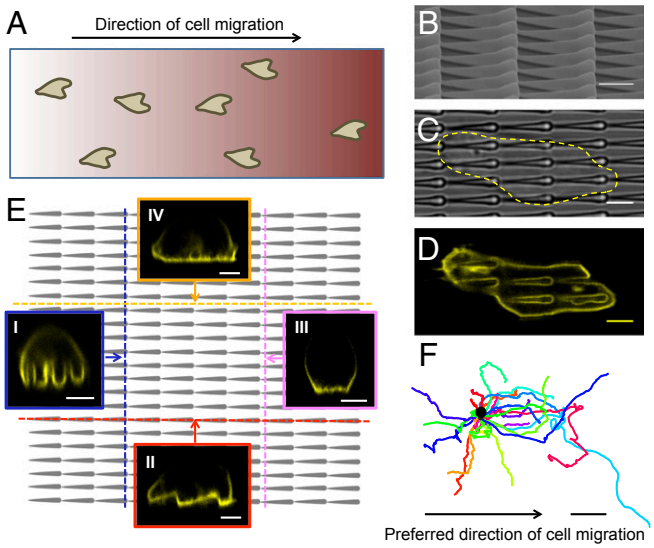

Fig. 1. Guidance of cells by a global gradient, e.g., in classic chemotaxis (*A*) and by a surface with 2-μm-spaced ridges of sawteeth of length 6 μm, height 1.8 μm, and width 630 nm (*B–F*). (*A*) A global gradient must be maintained over a distance that is much larger than the cell length. (*B*) Side-view scanning electron micrograph of sawteeth. (*C* and *D*) Top-view bright-field (*C*) and confocal (*D*) micrographs of a cAR1-YFP–expressing cell on sawteeth. The dashed line in *C* delineates the cell boundary. (*E*) Side-view confocal micrographs of different cross-sections of a cAR1-YFP–expressing cell on sawteeth. The gray background schematic represents the sawtooth surface. Each image was obtained at a plane perpendicular to the surface in the position of the dashed line of the color of the image border. (Scale bars: *B–E*, 3 μm.) (*F*) Centroid motion tracks of 25 representative cells over 18 min. All tracks were translated to begin at the black dot. The height of each sawtooth increases from left to right. (Scale bar: 20 μm.)

a fluorescent transmembrane protein that is uniformly distributed in the plasma membrane (23). Fig. 1 *D* and *E* show top- and side-view fluorescent confocal images, respectively, of an individual cell on a sawtooth surface. The sawtooth boundary highlighted in the top-view image indicates that the cell membrane is in contact with the entire surface of each sawtooth, leading to an apparently thicker plasma membrane around the sawteeth and hence an increased cAR1-YFP density. Side-view images confirm that cells conform to the deepest and highest positions of sawteeth.

To eliminate the possibility that cells are guided by chemical signals emitted by other cells, we imaged signal-relay-deficient *aca*$^{-}$ *D. discoideum* cells. We studied these cells under the conditions in which they are most capable of following a chemical gradient (starvation for 5 h), but we did not apply an external chemical gradient in our studies of microthigmotaxis. The cytoplasm was dyed with cellTracker Green (7) to enable tracking of centroid motion. Representative tracks (Fig. 1*F*) exhibit substantial unidirectional bias up the sawtooth slope.

To quantify the unidirectional bias, we analyzed cellular velocity with respect to the orientation of 2-μm-spaced ridges composed of sawteeth either 8 μm long, 2.4 μm high, and 630 nm wide (denoted as 8-μm sawteeth) or 2 μm long, 1 μm high, and 630 nm wide (denoted as 2-μm sawteeth). The polar histogram (Fig. 2*A*) and the probability distribution (Fig. 2*B*) of the direction of motion on 8-μm sawteeth demonstrate bias of motion up the sawtooth slope. There is also a slight preference for motion along the 90–270° axis. This minor component of directional bias arises because the sawtooth ridges are in registry, and so the sawtooth minima act as grooves that are perpendicular to the ridges. The slowest cells exhibit the smallest degree of directional preference in their migration (Fig. 2*D*). Furthermore, the most elongated cells show the greatest alignment with the ridges (Fig. 2*E*). We also analyzed cell motion on 2-μm-spaced ridges composed of sawteeth that are 6 μm long, 1.8 μm high, and 630 nm wide (the sawteeth shown in Fig. 1) with the same metrics; the results are similar to those of cell motion on 8-μm sawteeth. In contrast, the preferred direction on 2-μm sawteeth is down the sawtooth slope (Fig. 2 *F–J*). These results illustrate that the direction of microthigmotaxis is dependent on the details of the nano/microtopography.

For further assessment of the relationship between the guidance direction and the frequency at which the cell encounters the sawteeth, it would be desirable to study cell motion on surfaces in which the sawtooth length is 1 μm or smaller. However, because of the constraints of our fabrication method, it is difficult to fabricate asymmetric sawteeth with lengths of 1 μm or less. Instead, we fabricated sawtooth surfaces with an offset configuration in which the adjacent ridges are out of phase at a constant distance. Microthigmotaxis was monitored on such surfaces featuring 800-nm-spaced ridges of sawteeth of length 2 μm, height 400 nm, and width 400 nm (Fig. S1 *A* and *B*). Sawteeth in adjacent ridges were offset by 1 μm. Because of this offset, a cell encounters one new tooth for every 1 μm of displacement. The spacing between ridges was reduced from 2 μm to 0.8 μm to provide each cell with more guidance cues. The probability distribution of direction of motion (Fig. S1*C*) indicates that cells tend to migrate parallel to the ridges and down the sawteeth.

We next consider how the sawteeth influence intracellular dynamics. Snapshots of the spatial distribution and dynamics of actin filaments (F-actin) using cells that overexpress proteins associated with actin polymerization (LimEΔcoil-GFP and LifeAct-TagRFP) show that F-actin forms streak-like linear structures parallel to the ridges of 8-μm sawteeth. These structures extend 500 nm away from the ridges. Time-lapse imaging reveals that the F-actin streaks are actin polymerization waves in which the leading tip of each streak sweeps to probe the nano/microenvironment (Movie S2). The linear actin structures that adhere to the opposite sides of a sawtooth typically exhibit coupled dynamics (Fig. 3 *A–C*). To confirm that the dynamic fluorescence arises from the in situ actin polymerization rather than from an optical effect, we imaged cAR1-YFP cells migrating on the nanosawtooth surface as a control. The fluorescence in the plasma membrane remains spatially uniform, with no apparent bursts of intensity enhancement or depletion (Movie S3).

To assess the role of the ridges in unidirectional contact guidance, cell motion was analyzed on a single sawtooth "ridge" with a width of 300 μm (i.e., a pattern akin to closed louvers). Cell motion on a film of 8-μm-long, 2.4-μm-high sawteeth (Fig. S2 *A* and *B*) exhibits a bidirectional bias along the perpendicular sawtooth grooves, whereas migration along the sawteeth is suppressed (Fig. S2*C*). Therefore, the existence of nano/microscale ridges is a prerequisite for achieving unidirectional guidance, presumably because the edges of ridges promote the streak-like polymerization of actin adhering to them.

We adapted an optical-flow algorithm to determine the direction and magnitude of the apparent flux of actin polymerization for each pixel. Although this flux has the same preferred direction as cell motion, actin polymerization is more strongly unidirectional than is cell migration (compare Figs. 2*B* and 3*D*). Because the actin polymerization exhibits directed, wave-like dynamics, we term this internal guidance phenomenon "esotaxis" (with "eso" being Greek for "inner"). Movie S2 shows that actin polymerization waves push on the leading edge of the portion of the plasma membrane that adheres to the surface, suggesting a causal relationship between the directed actin-wave propagation (esotaxis) and the directed cell motion (microthigmotaxis). Averaging of polymerization activity around each 8-μm sawtooth shows that sawtooth minima serve as sources of actin polymerization waves that propagate up the sawteeth (Fig. 3*E*). The actin waves have a uniform speed but sometimes stall at the tips of sawteeth (Fig. 3*F*); 2-μm sawteeth also induce localized waves that are confined along the tops of the sawteeth (Fig. 3 *G–L*), and yet in this case, the waves migrate preferentially down the sawtooth slope. The speed of actin waves is comparable in both cases, about 30 μm/min. This behavior is

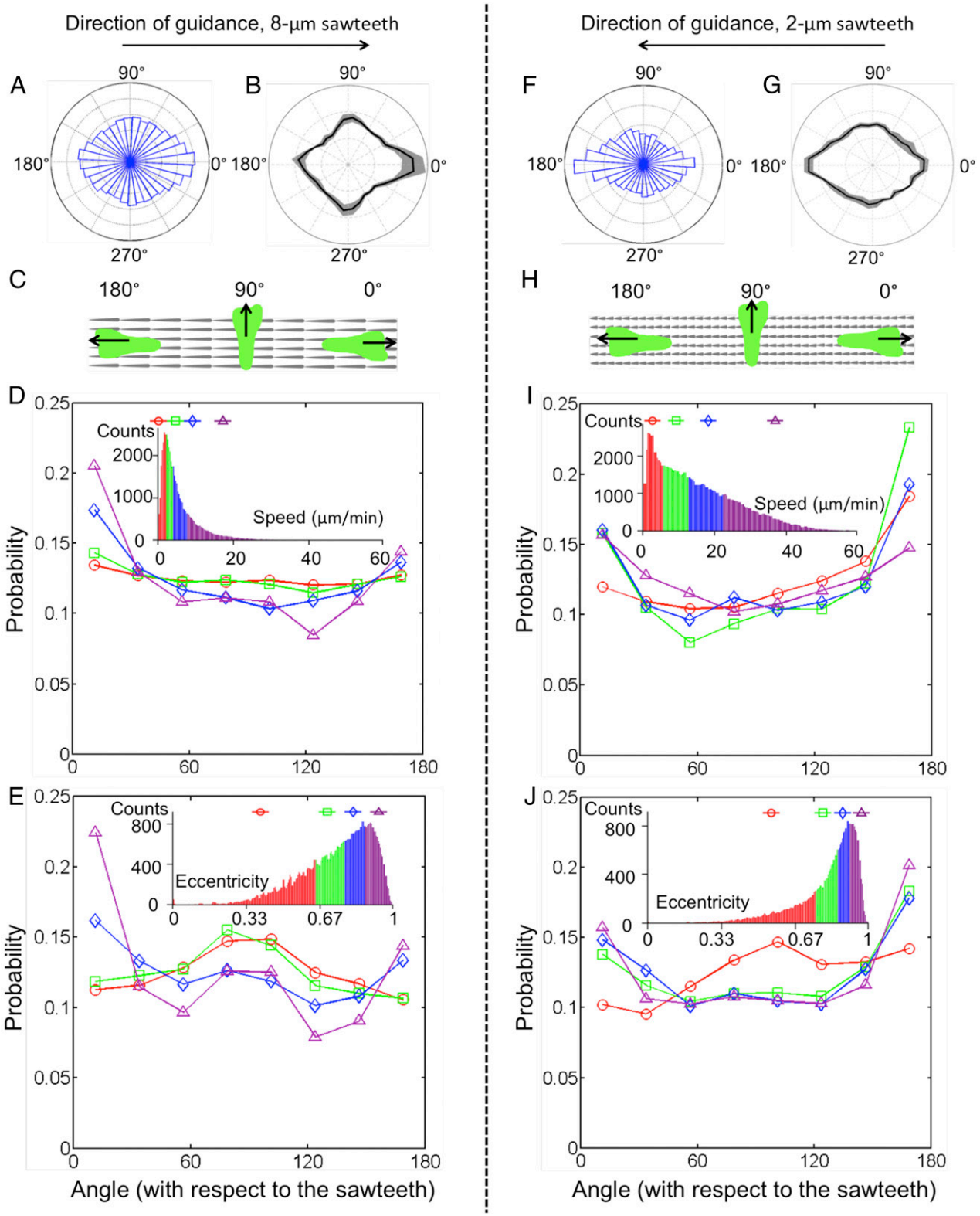

Fig. 2. Unidirectional cell migration is sensitive to details of the nano/microtopography. On 8-μm sawteeth, cells migrate up the slant (*A*–*E*), whereas on 2-μm sawteeth, they migrate down the slant (*F*–*J*). (*A* and *F*) Polar histograms of the direction of motion. (*B* and *G*) Probability distributions of the direction of motion weighted by speed. The solid line is an average over three experiments. The shaded area represents the SE. (*C* and *H*) Cartoons illustrate the definitions of the angles used to describe cell motion relative to the sawteeth. (*D* and *I*) Probability densities of cellular velocity with respect to the sawtooth orientation. *Inset* shows the speed distribution and range for each quartile. (*E* and *J*) Probability densities of cellular alignment with respect to the sawtooth orientation. The alignment direction is corrected by the direction of motion. *Insets* show the eccentricity distribution and range for each quartile.

consistent with the observed cell motion. As was the case for 8-μm sawteeth, actin polymerization is more strongly biased than is migration for 2-μm sawteeth (compare Figs. 2*G* and 3*J*).

The actin waves we observe are presumably different from those recently found in connection with phagocytosis/micropinocytosis (24–26), because phagocytosis/micropinocytosis is suppressed after 5 h of development (27). To assess directly whether phagocytosis/macropinocytosis plays a role in the observed unidirectional actin-wave propagation, we inhibited PI3K, which is required in phagocytosis/macropinocytosis, by incubating the developed cells with LY294002. The actin-flux analysis still shows a unidirectional bias up the slope (Fig. S3 *A* and *B*), indicating that the unidirectional guidance we observe is independent of phagocytosis/macropinocytosis.

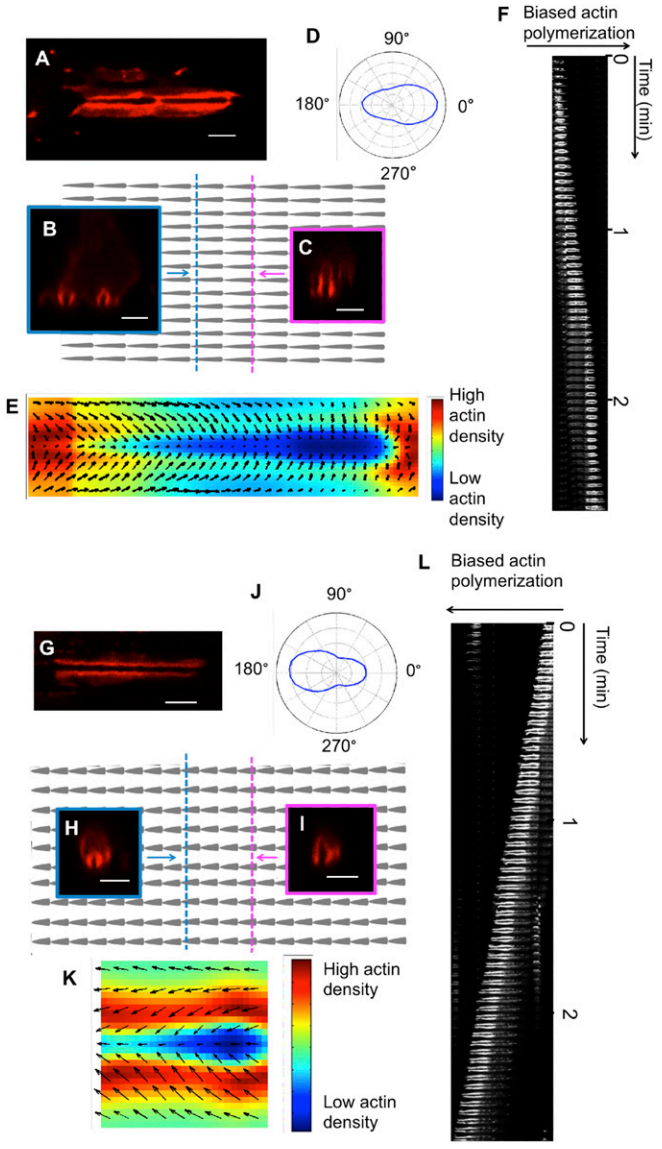

Fig. 3. Actin morphology and flux for *D. discoideum* depend on details of the nano/microtopography. (*A*–*L*) Eight-micron sawteeth (*A*–*F*) and 2-μm sawteeth (*G*–*L*). (*A* and *G*) Top-view confocal micrographs of F-actin on sawteeth. (*B*, *C*, *H*, and *I*) Confocal micrographs of cross-sections perpendicular to the ridges going through the sawtooth minima (*B* and *H*) and maxima (*C* and *I*). (*D* and *J*) Actin-wave directionality. (*E* and *K*) Average actin flux around a sawtooth. (*F* and *L*) Sixty-frame (2.55-min) space/time plot of actin waves along a ridge. (Scale bars: *A*–*C* and *G* and *I*, 3 μm; *F*, 16 μm; *L*, 4 μm.)

We also studied actin-wave propagation in human neutrophils (YFP–actin HL60). Unlike *D. discoideum*, which protrudes pseudopods that can be microns above the surface, neutrophils extend lamellipodia (Fig. 4 *A* and *B*) that adhere firmly to the surface. The actin-wave dynamics in HL60 cells on sawteeth are similar to those of *D. discoideum*, even though actin waves in HL60 cells are localized in lamellipodia, whereas actin waves in *D. discoideum* occur throughout the area of cell-surface contact. HL60 cells on 8-μm sawteeth exhibit unidirectional bias of actin waves and migrate up the sawteeth (Fig. 4*C* and Movie S4). Individual actin waves undergo persistent propagation along multiple sawteeth (Fig. 4*D*). The average speed of actin waves in HL60 cells is faster when the waves are propagating up the sawteeth than when they are propagating down the sawteeth (Fig. 4*E*) and is significantly slower than in *D. discoideum*. Actin waves in HL60 cells on 2-μm sawteeth exhibit bidirectional guidance (Fig. 4*F*). The speed of the actin waves on 2-μm sawteeth is significantly slower than that on 8-μm sawteeth (Fig. 4*G*).

Conclusions

Our results demonstrate unambiguously that unidirectional guidance can be achieved by local nano/microtopographical gradients on scales smaller than that of a single cell, but comparable to typical sizes of collagen fibers. The directed cellular motion (microthigmotaxis) arises from directed, internal actin-wave propagation (esotaxis). Here, nano/microtopography guides intracellular dynamics (waves of actin polymerization), propelling the cell with a preferred direction. However, it should also be noted that suitable microscopic patterns in properties such as surface chemistry or elastic modulus could potentially also induce esotaxis. The dependence of the guidance direction on sawtooth length and height indicates that multiple competing mechanisms may be involved in biasing actin polymerization waves. Some of the factors that affect actin polymerization are presumably sensitive to local geometry. Such factors may include membrane tension, which locally inhibits actin polymerization (28), and bending of actin filaments, which leads to preferred localization of the Arp 2/3 complex on the convex side of bent actin filaments (29). The conservation of microthigmotaxis and esotaxis for different cell types with distinct surface interactions during migration and the prevalence of polarity and asymmetry in the local microenvironment of cells suggest that biasing of intracellular waves is important in many physiological processes. For instance, aligned collagen fibers guide cancer cells and are a prognostic signature of breast carcinoma (30). Our results suggest the possibility that asymmetric nano/microtopography of collagen fibers promotes unidirectional contact guidance in vivo. Asymmetric topographies could be incorporated in tissue engineering and regenerative medicine. For instance, sawtooth surfaces may be used to accelerate the wound-healing process by promoting the unidirectional migration of neutrophils, fibroblasts, and epithelial cells toward the injured site. Controlled anisotropic nano/microtopographies imprinted on surfaces or embedded in 3D structures should be able to guide cells over large distances, with possible applications in the broad range of biomedical problems in which directed cell migration is important.

Materials and Methods

Preparation of Sawtooth Surfaces. Sets of parallel, 300-μm-long ridges of asymmetric sawteeth were fabricated via multiphoton absorption polymerization (MAP) (31) using a commercial Ti:sapphire laser (Coherent Mira 900-F). Each set covered an area of 300 × 300 μm. Surfaces composed of continuous nanosawteeth (as opposed to ridges of sawteeth) were fabricated with a 200-nm step size perpendicular to the sawteeth. The acrylic resin used was composed of 49 wt% Tris(2-hydroxyethyl) isocyanurate triacrylate (SR368; Sartomer), 49 wt% ethoxylated (6) trimethylolpropane triacrylate (SR499; Sartomer), and 2 wt% Lucirin TPO-L (Ciba). Master structures were fabricated on acrylate-functionalized glass slides (32). The typical power of the fabrication beam was 4 mW as measured at the sample. The sample preparation and fabrication procedure have been described previously (32). The master surfaces were functionalized

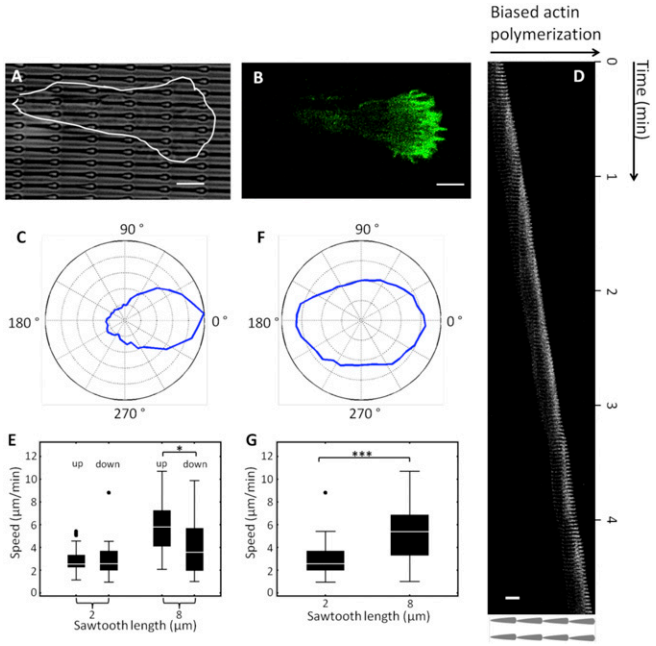

Fig. 4. Cellular morphology and actin waves of YFP-actin HL60 neutrophils on sawteeth. (*A* and *B*) Bright-field micrograph (*A*) and confocal micrograph (*B*) of a polarized neutrophil. (*C* and *F*) Directionality of actin waves on 8-μm sawteeth (*C*) and 2-μm sawteeth (*F*). (*D*) Space/time plot of actin waves along a ridge over 146 frames (4.83 min). (*E* and *G*) Actin-wave propagation speed. $*P \leq 0.05$; $***P \leq 0.001$. (Scale bars: *A* and *B*, 4 μm; *D*, 8 μm.)

with primary amines using a mixture of ethylenediamine (E26266; Sigma-Aldrich) and ethanol (1:4, vol/vol) for 30 min, and then were treated with a solution containing 0.03 g of perfluorooctadecanoic acid (L16837; Alfa Aesar), 4.5 g of hexafluorobenzene (H8706; Sigma-Aldrich), 16 mL of ethanol, and 50 μL of methanol for 1.5 h to render the surface highly hydrophobic, facilitating the release of cured polydimethylsiloxane (PDMS). To replicate sawteeth accurately, we modified a previously described method (33) to prepare a composite PDMS mold consisting of a thin layer of hard PDMS with relief features that was backed by a thick slab of soft PDMS. To prepare the hard PDMS, 1.7 g of vinyl PDMS prepolymer (VDT-731; Gelest), 9 μL of Pt catalyst (SIP6831.2; Gelest), 0.05 g of modulator (87927; Sigma-Aldrich), 0.5 g of hydrosilane (HMS-301; Gelest), and 1 g of hexane were mixed. The mixture was spin-coated on the master surface (1,000 rpm, 40 s), allowed to sit at room temperature for 2 h, and then baked at 60 °C for 1 h. Soft PDMS was prepared by mixing the base and curing agent (Sylgard 184; Dow Corning) in a 10:1 mass ratio. After degassing, the uncured soft PDMS was poured onto the precured hard PDMS and baked at 60 °C for 1 h. After curing, the composite PDMS was peeled off of the master surface. Replicas of sawteeth were created by sandwiching a drop of acrylic resin between the mold and an acrylate-functionalized coverslip and then UV curing (Blak-Ray, B-100AP, 100 W, 365 nm; samples were cured 254 mm from the source). Surfaces for *D. discoideum* were UV-cured for 5 min and then treated with high-pressure oxygen plasma for 3 min. Surfaces for neutrophils were UV cured for 40 s, baked at 90 °C for 10 min, and then coated with 1 μg/mL fibronectin in HBSS [F1141 (Sigma-Aldrich); fluorescent fibronectin: FNR02-A (Cytoskeleton)] at 37 °C for 1 h. The coated surface exhibited uniform fibronectin density (Movie S5).

To prepare the fluorescent sawteeth for confocal *z*-stack imaging (Movie S1), 2 wt% Rhodamine B was added into the acrylic resin. After thorough mixing, the resin was filtered through a 200-nm-pore-size syringe filter. The replica was prepared in the same way as described above.

Cell Preparation and Imaging. *D. discoideum* cells, cAR1-YFP, *aca*$^-$, LimEΔcoil-GFP, and Lifeact-TagRFP/*aca*$^-$ (all are in an AX3 background) were prepared as described previously (7). cAR1-YFP and LimEΔcoil-GFP cells were developed for 4 h. *aca*$^-$ and Lifeact-TagRFP/*aca*$^-$ cells were developed for 5 h.

cAR1-YFP cells were incubated with 2 mM caffeine for 20 min to block the intracellular activation of cAMP synthesis (34). After being plated onto a sawtooth surface, cells were stimulated with exogenous cAMP with a uniform concentration of 5 μM. Fluorescence images were obtained on a Leica SP5 X confocal microscope every 2 s with a 100× objective and a scanner zoom factor of 2.

For cell motion imaging, *aca*$^-$ cells were cytoplasmically dyed with 25 μM CellTracker Green CDMFA (5-chloromethylfluorescein diacetate) (Invitrogen) for 30 min and then washed twice with phosphate buffer. After being plated onto a sawtooth surface, cells were stimulated with exogenous cAMP with a uniform concentration of 100 nM. Fluorescence images of *aca*$^-$ cells were obtained on a Leica TCS SP2 confocal microscope every 4 s for 80 min with a 10× objective and a scanner zoom factor of 2. Images were obtained in a 512 × 512 pixel format.

For actin-wave imaging, LimEΔcoil-GFP cells were incubated with 2 mM caffeine for 20 min after development. LimEΔcoil-GFP and Lifeact-TagRFP/*aca*$^-$ cells were stimulated with exogenous cAMP with a uniform concentration of 5 and 100 nM, respectively. Both fluorescence and bright-field images were obtained simultaneously on a Leica SP5 X confocal microscope every 2.6 s with a 100× objective and a scanner zoom factor of 2. Images were obtained in a 1,024 × 1,024 pixel format to provide more information for actin-flux analysis.

To inhibit PI3K in Lifeact-TagRFP/*aca*$^-$ *D. discoideum* cells that have been developed for 5 h, we incubated the cells with both 10 μM and 50 μM LY294002, and stimulated the cells with exogenous cAMP with a uniform concentration of 3 μM. Both fluorescence and bright-field images were obtained simultaneously on a Leica SP5 X confocal microscope every 2.6 s with a 100× objective. Images were obtained in a 1,024 × 1,024 pixel format.

The neutrophil-like human leukemia cell line HL60 overexpressing YFP-actin was a kind gift of Orion Weiner (University of California, San Francisco, CA). Cells were maintained in RPMI 1640 (medium developed at Roswell Park Memorial Institute) with Glutamax (Invitrogen), 10% (vol/vol) FBS, and penicillin/streptomycin. Cells were passaged every 3–4 d to maintain a density between 10^5 cells/mL and 10^6 cells/mL. Cells were differentiated at a density of 4.5×10^5 cells/mL for 6 d in culture medium containing 1.3% (vol/vol) dimethyl sulfoxide. Before imaging, cells were plated on a sawtooth surface coated with 1 μg/mL fibronectin and stimulated with 1 μM f-Met-Leu-Phe (fMLP) in mHBSS (Hank's Balanced Salt Solution) for 10 min. Fluorescence and bright-field time-lapse images were obtained on a Leica SP5 X confocal microscope every 2 s with a 100× objective.

Tracking Cells. Migrating *D. discoideum* cells were tracked as previously described (7, 17). Because of image noise, even stationary cells appear to have a direction of motion. We therefore measured the distribution of direction of motion in two different ways: a simple histogram of direction of motion (e.g., Fig. 2 *A* and *E*) and a probability distribution of direction of motion weighted by speed (e.g., Fig. 2 *B* and *F*). The weighted plots show the net speed of cells moving in each direction. In all plots, each included speed corresponds to that of a cell in a specific frame rather than the mean speed of a single cell averaged across time.

We also plotted the velocity direction distributions (unweighted) for each speed quartile (e.g., Fig. 2 *D* and *I*) and the orientation distributions for each eccentricity quartile (e.g., Fig. 2 *E* and *J*). Angles were defined relative to the sawtooth orientation; a cell migrating 5° to the right of the direction up the sawteeth and a cell migrating 5° to the left of the direction up the sawteeth would both be described as migrating at 5° relative to the sawtooth orientation. The alignment and eccentricity of cells were calculated as described previously (17). We calculated the cell orientation, which ranges from 0° to 360°, from the cell alignment, which ranges from 0° to 180°, using the direction of cellular motion. From the two possible orientations that correspond to each alignment, the orientation was chosen that was closest to the direction of the cell. Additionally, all quartile plots were scaled so that the sum of all angular bins was unity.

Tracking Actin Polymerization. In *D. discoideum* and neutrophils, actin polymerization occurs in reaction–diffusion–type waves. To measure the directionality of these polymerization waves, we used a modified optical-flow algorithm. Optical-flow algorithms assign a pixel-dependent apparent velocity in an image sequence. At each pixel, our algorithm assigns a direction of actin-wave polymerization and a quantity of newly polymerized actin. Although the algorithm does not track stationary actin foci, stationary regions of actin polymerization are included in the unit-cell analysis described below.

To adjust for differences in protein expression levels from cell to cell, all *D. discoideum* and neutrophil images were γ-corrected using a γ of 0.5 before calculating the difference images. A γ correction of 0.5 deemphasizes differences between high intensities, while maintaining differences between low intensities. Cells express different levels of LimEΔcoil-GFP and so have different average intensities. Applying a γ correction before further analysis thus allows us to "count" cells of differing brightness more equally without destroying the contrast between the background and dim cells. To track actin polymerization across a pair of subsequent frames, f_t and f_{t+1}, we first found the difference image $f_{t+1} - f_t$. Then, to reduce noise, the difference image was smoothed with a Gaussian filter of SD 3 pixels for *D. discoideum* and 1 pixel for neutrophils. Intensity values in our images ranged from 0 to 255. For further noise reduction, a lower threshold of 43

was applied for *D. discoideum* and 24 for neutrophils. Different parameters were used for the analysis of *D. discoideum* and neutrophils, because these cell types migrate at different speeds and were imaged at different resolutions. The intensity of each pixel in this difference image was assumed to be proportional to the amount of newly polymerized actin. To associate a direction with the newly polymerized actin at each pixel, an actin polymerization wave was assumed to be most likely to come from the direction of greatest newly polymerized actin in the previous difference image. Similarly, it is expected that the newly polymerized actin is most likely to travel toward the direction of greatest newly polymerized actin in the future difference image. Therefore, the previous difference image, $f_t - f_{t-1}$, and the future difference image, $f_{t+2} - f_{t+1}$, were then found. Both difference images were then smoothed with Gaussian filters of SD 5 pixels for *D. discoideum* and 3 pixels for neutrophils. This smoothing step spreads information about the previous and future newly polymerized actin to the location of the newly polymerized actin in the current difference image. The SD of the filter in this smoothing determines the speed of the fastest actin wave that can be tracked by the algorithm. In addition to reducing noise, the first smoothing and the lower threshold described above determine the speed of the slowest actin wave that can be tracked by the algorithm. Finally, we associated a direction with the newly polymerized actin by subtracting the normalized gradient of the previous difference image from the normalized gradient of the future difference image.

Averaged Actin-Flux Analysis. We measured the mean actin fluorescence and actin flux around a sawtooth by averaging across the sawteeth in a movie. To locate the sawteeth, cells were imaged simultaneously in fluorescence and bright-field modes. The sawtooth orientation, ridge spacing, and sawtooth length were measured in each bright-field image. First, a Radon transform (35) with an angular step size of 0.1 degrees was used to find the sawtooth orientation. Each bright-field image was then rotated such that the sawteeth were aligned horizontally. The image edges were discarded, because they exhibit interpolation artifacts due to the rotation. Next, each image was projected onto the vertical and horizontal axes. To measure the ridge spacing and sawtooth length to subpixel accuracy, each projection was interpolated using a cubic spline with a spacing of 0.1 pixels. The spacing and pitch were then measured from the autocorrelations of the splines. The spacing was measured from the vertical projection, which is in the direction perpendicular to the ridges, and the pitch was measured from the horizontal projection, which is in the direction parallel to the ridges.

The actin fluorescence intensity and actin flux were next averaged across all of the sawteeth. Each fluorescence image was rotated so that the sawteeth were horizontal. The actin-flux measure was similarly rotated, as was the angle of the vectors within the field. Next, the images were enlarged using a bilinear interpolation, such that the ridge spacing and sawtooth length would be of the next greatest integer size. For instance, if the ridge spacing were 26.8 pixels, then the corresponding dimension of the image would be enlarged by the factor 27/26.8. Forcing the ridge spacing and sawtooth length to have integer dimensions allows for simple averaging across multiple sawteeth. Within each image, the averages of the measures around each sawtooth were next found by tiling the image into subimages of sawtooth size and averaging across the subimages. The mean measures were averaged across images by using the positions of the sawteeth tips in the bright-field images as a guide. To align the sawteeth to subpixel scale, all of the averaged measures were first enlarged by a factor of eight. The bright-field averaged image was then blurred using a Gaussian filter with a SD of 16 pixels. Next, the sawtooth tip was found in the direction parallel to the ridges by finding the row with the greatest SD in bright-field intensity. The position of the tip parallel to the ridges was then found as the position with the greatest bright field intensity along the ridge. After centering, the mean measures were shrunk by a factor of eight and then averaged across all frames.

Measuring Actin-Wave Speed. The actin-wave propagation speed in neutrophils (Fig. 4 *E* and *G*) was measured using space/time plots (Fig. S4). An actin wave traveling along a single ridge was cropped and resized into a single-pixel width using the ImageJ software (National Institutes of Health) (36). The same processing was repeated on every cropped image in the time-lapse series. The resized actin waves were montaged into a space/time plot. Actin-wave propagation speed was obtained by dividing the distance that the wave front traveled by the time lapse. More than 60 individual speeds were measured on each type of sawtooth surface.

ACKNOWLEDGMENTS. We acknowledge Dr. Nikos Liaros for helping us with Greek. Support from National Institutes of Health (NIH) Grant R01GM085574 is gratefully acknowledged. X.S. was partially supported by the Graduate Dean's Dissertation Fellowship. We appreciate the support of the Maryland NanoCenter and its NispLab. The NispLab is supported in part by the National Science Foundation as an Materials Research Science and Engineering Center Shared Experimental Facility. Part of this research was supported by the Intramural Research Program of the Center for Cancer Research, National Cancer Institute, NIH.

1. Ridley AJ, et al. (2003) Cell migration: Integrating signals from front to back. *Science* 302(5651):1704–1709.
2. Doitsidou M, et al. (2002) Guidance of primordial germ cell migration by the chemokine SDF-1. *Cell* 111(5):647–659.
3. Farooqui R, Fenteany G (2005) Multiple rows of cells behind an epithelial wound edge extend cryptic lamellipodia to collectively drive cell-sheet movement. *J Cell Sci* 118(Pt 1):51–63.
4. Ding Y, Xu J, Bromberg JS (2012) Regulatory T cell migration during an immune response. *Trends Immunol* 33(4):174–180.
5. Seo Y-K, et al. (2009) Increase in cell migration and angiogenesis in a composite silk scaffold for tissue-engineered ligaments. *J Orthop Res* 27(4):495–503.
6. Parent CA, Devreotes PN (1999) A cell's sense of direction. *Science* 284(5415):765–770.
7. McCann CP, Kriebel PW, Parent CA, Losert W (2010) Cell speed, persistence and information transmission during signal relay and collective migration. *J Cell Sci* 123(Pt 10):1724–1731.
8. Lo C-M, Wang H-B, Dembo M, Wang YL (2000) Cell movement is guided by the rigidity of the substrate. *Biophys J* 79(1):144–152.
9. Cattaruzza S, Perris R (2005) Proteoglycan control of cell movement during wound healing and cancer spreading. *Matrix Biol* 24(6):400–417.
10. Kriebel PW, Barr VA, Parent CA (2003) Adenylyl cyclase localization regulates streaming during chemotaxis. *Cell* 112(4):549–560.
11. Afonso PV, et al. (2012) LTB4 is a signal-relay molecule during neutrophil chemotaxis. *Dev Cell* 22(5):1079–1091.
12. Décave E, et al. (2003) Shear flow-induced motility of Dictyostelium discoideum cells on solid substrate. *J Cell Sci* 116(Pt 21):4331–4343.
13. Décavé E, Garrivier D, Bréchet Y, Fourcade B, Bruckert F (2002) Shear flow-induced detachment kinetics of Dictyostelium discoideum cells from solid substrate. *Biophys J* 82(5):2383–2395.
14. Wójciak-Stothard B, Madeja Z, Korohoda W, Curtis A, Wilkinson C (1995) Activation of macrophage-like cells by multiple grooved substrata. Topographical control of cell behaviour. *Cell Biol Int* 19(6):485–490.
15. Diehl KA, Foley JD, Nealey PF, Murphy CJ (2005) Nanoscale topography modulates corneal epithelial cell migration. *J Biomed Mater Res A* 75(3):603–611.
16. Doyle AD, Wang FW, Matsumoto K, Yamada KM (2009) One-dimensional topography underlies three-dimensional fibrillar cell migration. *J Cell Biol* 184(4):481–490.
17. Driscoll MK, Sun X, Guven C, Fourkas JT, Losert W (2014) Cellular contact guidance through dynamic sensing of nanotopography. *ACS Nano* 8(4):3546–3555.
18. Wang J, Petefish JW, Hillier AC, Schneider IC (2015) Epitaxially grown collagen fibrils reveal diversity in contact guidance behavior among cancer cells. *Langmuir* 31(1):307–314.
19. Bretschneider T, et al. (2004) Dynamic actin patterns and Arp2/3 assembly at the substrate-attached surface of motile cells. *Curr Biol* 14(1):1–10.
20. Giannone G, et al. (2004) Periodic lamellipodial contractions correlate with rearward actin waves. *Cell* 116(3):431–443.
21. Gerisch G, et al. (2004) Mobile actin clusters and traveling waves in cells recovering from actin depolymerization. *Biophys J* 87(5):3493–3503.
22. Weiner OD, Marganski WA, Wu LF, Altschuler SJ, Kirschner MW (2007) An actin-based wave generator organizes cell motility. *PLoS Biol* 5(9):e221.
23. Xiao Z, Zhang N, Murphy DB, Devreotes PN (1997) Dynamic distribution of chemoattractant receptors in living cells during chemotaxis and persistent stimulation. *J Cell Biol* 139(2):365–374.
24. Clarke M, et al. (2010) Curvature recognition and force generation in phagocytosis. *BMC Biol* 8:154.
25. Gerisch G, et al. (2009) Self-organizing actin waves as planar phagocytic cup structures. *Cell Adhes Migr* 3(4):373–382.
26. Veltman DM, Lemieux MG, Knecht DA, Insall RH (2014) PIP_3-dependent macropinocytosis is incompatible with chemotaxis. *J Cell Biol* 204(4):497–505.
27. Katoh M, Chen G, Roberge E, Shaulsky G, Kuspa A (2007) Developmental commitment in Dictyostelium discoideum. *Eukaryot Cell* 6(11):2038–2045.
28. Houk AR, et al. (2012) Membrane tension maintains cell polarity by confining signals to the leading edge during neutrophil migration. *Cell* 148(1-2):175–188.
29. Risca VI, et al. (2012) Actin filament curvature biases branching direction. *Proc Natl Acad Sci USA* 109(8):2913–2918.
30. Conklin MW, et al. (2011) Aligned collagen is a prognostic signature for survival in human breast carcinoma. *Am J Pathol* 178(3):1221–1232.
31. LaFratta CN, Fourkas JT, Baldacchini T, Farrer RA (2007) Multiphoton fabrication. *Angew Chem Int Ed Engl* 46(33):6238–6258.
32. Stocker MP, Li L, Gattass RR, Fourkas JT (2011) Multiphoton photoresists giving nanoscale resolution that is inversely dependent on exposure time. *Nat Chem* 3(3):223–227.
33. Kang H, Lee J, Park J, Lee HH (2006) An improved method of preparing composite poly(dimethylsiloxane) moulds. *Nanotechnology* 17:197–200.
34. Brenner M, Thoms SD (1984) Caffeine blocks activation of cyclic AMP synthesis in Dictyostelium discoideum. *Dev Biol* 101(1):136–146.
35. Deans SR (2007) *The Radon Transform and Some of Its Applications* (Dover Publications, Mineola, NY).
36. Collins TJ (2007) ImageJ for microscopy. *Biotechniques* 43(1 Suppl):25–30.